C2FUEL - This project has received funding from the European Union's Horizon 2020 research and innovation programme under grant agreement No 838014

C2FUEL

Carbon Captured Fuel and Energy Carriers for an Intensified Steel Off-Gases based Electricity Generation in a Smarter Industrial Ecosystem

Deliverable

D4.3 – Analysis of reactor types in combination with different catalysts

WP4 – Development and upscale of FA production

Project information

Grant Agreement n°	838014
Dates	1st June 2019 – 30th November 2023

Document Status

Document information

Deliverable name	Analysis of reactor types in combination with different catalysts
Responsible beneficiary	TUE
Contributing beneficiaries	TUE
Contractual delivery date	M35 – 30/04/2022
Actual delivery date	M38 – 11/07/2022
Dissemination level	Confidential

Document approval

Name	Position in project	Organisation	Date	Visa
L. NAIGLIN	Project Management Officer	BENKEI	11/07/2022	OK
P. OLIVIER	Project Management Officer	ENGIE	08/07/2022	OK
M.C. Figueiredo	WP LEADER	TU/e	06/07/2022	OK

Document history

Version	Date	Modifications	Authors
V1	22/4/2022	1st version	A. de Leeuw den Bouter/TUE
V2	28/4/2022	Comments	J.van der Schaaf/TUE
V3	20/5/2022	2nd version	A. de Leeuw den Bouter/TUE
V4	7/6/2022	Comments	J.van der Schaaf/TUE
V5	27/6/2022	3rd version	A. de Leeuw den Bouter/TUE
V6	04/7/2022	Removal of non-public information	A. de Leeuw den Bouter/TUE
VF	11/07/2022	Quality check and final version	L. Naiglin / BENKEI

Table of Contents

List of Figures

List of Tables

Deliverable report

1 Executive Summary

1.1 Description of the deliverable content and purpose

In search for new sources for products and energy storage, attempts are made to use the waste product CO_2 as a source for valuable chemicals[1]. Formic acid is one such molecule that is widely used as feedstock in chemical industry[2] and is promising as a hydrogen carrier for energy storage, dispatch and on demand production[3] Formic acid can be produced using renewable energy and CO_2 from air. WP4 aims to develop a lab-scale formic acid (FA) production demonstrator that will produce sustainable formic acid by using H_2 (from SOEC) or H_2O, electrons and CO_2. The purpose of this deliverable is to perform a review of possible reactor types for the direct hydrogenation of CO_2 to formic acid, while looking in particular to the construction costs, complexity, lifespan and scalability. To this end, two different reactor types were studied: a conventional trickle bed reactor and a rotor-stator Spinning Disc Reactor (rs-SDR), with a final production target of 200 kton/year.

The design strategy followed within this deliverable is based on a traditional process design strategy following a hierarchy of activities, each dependent on the successive layer before it. This strategy is often illustrated using an *Onion Diagram*, as shown in Figure 1.

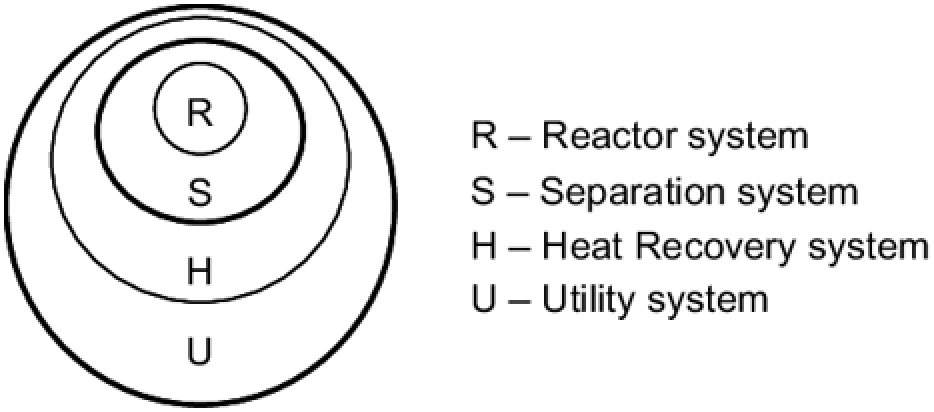

Figure 1 : Schematic representation of the Onion Diagram describing the followed process design hierarchy

In short, the design starts with the chemical reactor, after which the separation section is designed in order to obtain the desired product purities. When the design of the reactor and accompanying separation train is finalized, one can continue with the optimization of the heat recovery system and the utility system.

To this end, the process hierarchy of the *Onion Diagram* was employed: 1D-phenomenological reactor models were developed and to upscale and integrate the reactor design in an industrial scale process, these models were integrated in Aspen Plus V11.

Within this **Deliverable 4.3A** (further explanation on the separation of A and B versions can be found in section 1.3 - Corrective actions), the reactor modelling will be discussed. First, the 1D-phenomenological reactor model equations (i.e mass and energy balances) were implemented in MATLAB R2020a. To this end, kinetic models from literature were implemented, while adduct (FA:triaklylamine) stoichiometries were experimentally determined. The optimal operation conditions, maximizing the one-pass CO_2 conversion and FA yield. Afterwards, the reactors were upscaled to the desired production rate.

1.2 Brief description of the state of the art and the innovation breakthroughs

Nowadays a major search is on the way to develop a method to transform CO_2, which is often seen as a waste product due to anthropogenic emissions, into valuable chemicals [1]. Previous work has shown CO_2 can be transformed into a wide array of added-value chemicals by incorporation of alkanes, alkynes and epoxides [2]. Alternatively, CO_2 can also be used to store renewable energy in liquid fuels using hydrogen as an energy carrier [1][3], with examples being dimethyl ether (DME), and formic acid (FA) [1].

Formic acid is often seen as a promising organic molecule to store hydrogen, as it readily allows for a reversible transformation back to hydrogen and CO_2 besides being a valuable bulk chemical for preservatives and antibacterial agents [1]. Formic acid is known to store 4.3 wt% hydrogen and is liquid at ambient conditions, therefore allowing straightforward storage and transport [1], thus making formic acid a highly promising candidate as an energy carrier.

Though the number of heterogeneous catalysts for CO_2 hydrogenation to formic acid reported is yet relatively limited. The most popular active metals studied are Pd, Au and Ru on supports such as activated carbon, alumina and titania. Pd and Au are the most used catalysts, with the catalytic performance showing a strong dependency on the support material. Here, the most promising supports were found to be dependent on the active metal, with Pd preferring hydrophobic carbon-based supports, while Au should be combined with a hydrophilic support such as Al_2O_3 and TiO_2 [1][5]. Recently, promising results showing selectivity's > 99% were obtained by several research groups using gold based supported catalysts [6][7]. Within this deliverable, the kinetics models used are based on the commercial Au catalyst that was previously discussed within **Deliverable 4.2**, which is Au/Al_2O_3.

Even though the state-of-the-art catalysts seem sufficiently active and selective [1][4][5], the equilibrium concentrations reached remain low due to the reaction being thermodynamically unfavorable [4]. One of the commonly employed strategies is to reduce formic acid within the reaction mixture through the formation of adducts/complexes [4]. Often, nitrogenous bases or alkali is used for this purpose [4][5]. Promising results have been obtained using tertiary alkylamines, such as triethylamine [6][7]. Within this deliverable, the kinetics models used are based on the commercial Au catalyst and the usage of triethylamine as a reduction based, as was previously discussed within **Deliverable 4.2.**

In conclusion, the innovation of this project is based on the following main features:

- The use of CO_2 as carbon source for the synthesis of FA.
- The use of tertiary alkylamines to reduce formic acid within the reaction mixture, in order to shift the equilibrium and therefore overcome the thermodynamic limitations.
- The scale up of a fixed bed reactor and a spinning disc reactor, and the integration of these upscaled designs in an industrial scale process.

1.3 Corrective action (if relevant)

As mentioned before, **Deliverable 4.3** aims at the analysis of reactor types in combination with different catalysts and includes the assessment of the possible reactor technologies in order to evaluate the most promising technology. This delivery includes the validation and testing of the lab scale spinning disc reactor for direct CO_2 reduction and CO_2 hydrogenation as well as other competitive technologies. Due to problems on the specifications and delivery of the pressure regulators for the reaction setup, the experimental work for the completion of this deliverable is delayed. It is expected that the experimental part can be concluded in six months. However, to avoid further delays, and with specific agreement of the Project Officer, it was decided to submit **D4.3** in 2 parts, **D4.3A** containing all the results from the modelling and simulation on the different type of reactors (M38) and **D4.3B** containing the experimental results for the reactors (M42).

For the sake of confidentiality, some data have been removed from the present work. This is related to solubility of the gas in the adduct, and to stoichiometry of the adduct *vs* the amine. These data will be soon published. After that, an addendum will be made to this deliverable.

1.4 IPR issues (if relevant)

IP developed by TUE, licensing of models and designs will be considered.

2 Section 1 – Fixed bed reactor modelling and parameter optimization

2.1 Modelling approach and governing equations

Within industrial scale reactors, mass and/or heat transfer limitations can often occur, resulting in lower conversions than predicted by kinetic systems. In a regular fixed bed reactor, these mass and/or heat transfer limitations can occur at several length scales: within the catalyst particle (intra-particle mass/heat transfer limitations) and between the catalyst particle and the build fluid (external mass/heat transfer limitations). Within this deliverable, these different length scales will be studied for both the packed bed reactor as well as the rotor-stator Spinning Disc Reactor (rs-SDR). The modelling approach of each of these length scales will be discussed within the following sections.

At all length scales, the following assumptions were deemed valid:

1. Steady state conditions
2. 1D ideal plug flow: axial and radial heat and mass dispersion are neglected
3. The gas phase is considered an infinite reservoir
4. No pressure drop is considered, which entails a constant interstitial velocity in the axial direction both gas and liquid.
5. The CO_2 and H_2 concentration at the start of the column in the liquid phase is equal to saturation conditions
6. No phase separation between reactants and products at any length scale
7. The kinetic model is considered valid for both the fixed bed reactor as well as the rs-SDR
8. The catalyst particle can be a flat plate, cylindrical or spherical
9. Film theory is assumed to be valid
10. The catalyst remains stationary during operation
11. The liquid enters the column at saturation conditions
12. The catalyst is fully wetted

2.1.1 Particle scale

First, the governing equations and boundary conditions of the rigorous particle model are discussed. Within a particle model, the internal concentration and temperature profiles within a single catalytic particle can be studied. The particle model is used to evaluate the extent to which internal mass and/or heat transfer limitations play a role, allowing to design appropriate catalyst particles.

The particle model consists out of mass and energy balances. Within the catalyst particle the reactants need to diffuse in the catalyst pore to reach the active metal centers, while the products need to diffuse back through these pores to reach the bulk fluid. Convection was considered to be negligible at this scale. As stated before, the catalyst particle was assumed to operate at steady state, as no deactivation is known to occur for the production of formic acid from CO_2 based on previous works [5][9]. The steady state balance for any component I for any catalyst geometry is known to be:

$$0 = \frac{1}{r^v}\frac{\partial}{\partial r}\left(r^v\, D_{i,eff}\,\frac{\partial c_i}{\partial r}\right) - R_i$$

Here, r is the characteristic length of the catalyst particle, v the geometry factor (0 = flat plate, 1 = cylindrical, 2 = spherical), $D_{i,eff}$ the effective diffusivity of component i, c_i the molar concentration of component i and R_i the reaction rate of component I in terms of catalyst volume.

The coordinate system was chosen such that the particle center is the origin. At the center a finite concentration is enforced, also known as the symmetry boundary condition, in the form of a Neumann boundary condition:

$$\left.\frac{\partial c}{\partial r}\right|_{r=0} = 0$$

E4At the outer edge of the particle, where r = $R_{particle,}$, the concentration is equal to the fluid bulk concentration (Dirichlet boundary condition):

$$\left.\frac{\partial c}{\partial r}\right|_{r=R} = c_B$$

As the formation of formic acid from CO_2 is known to be exothermic, heat is generated by the reaction within the catalyst particle. Due to the close relation of mass and heat, the balances and boundary conditions are also very similar. The heat within the catalyst particle was assumed to only be governed by thermal conductivity, resulting in the following balance:

$$0 = \frac{1}{r^v}\frac{\partial}{\partial r}\left(r^v\, \lambda_{eff}\,\frac{\partial T}{\partial r}\right) + \sum \Delta H \cdot R_i$$

Here, the same definition are used as presented previously, with λ_{eff} the effective thermal conductivity and ΔH the reaction enthalpy. The reaction rate is a function of temperature following the Arrhenius approach. The boundary conditions employed are equal to those used within the mass balances. The particle model was subject to extensive verification based on irreversible first order reactions using a derived analytical expression, assuming a constant diffusivity. Two separate cases were studied, isothermal (flat plate geometry and spherical geometry) and non-isothermal. The results of the isothermal case can be found in Figure 2.

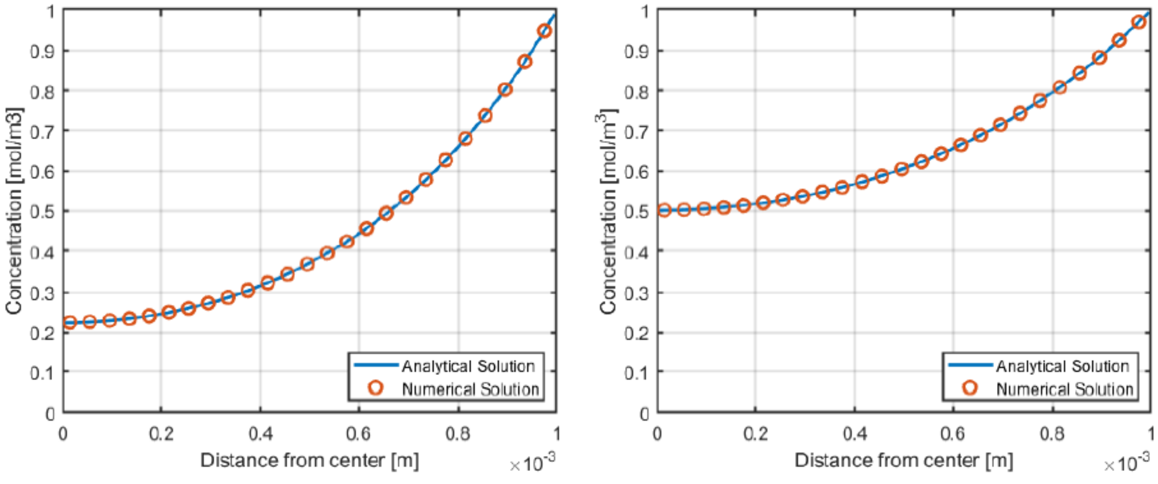

(a) Flat plate geometry. (b) Spherical geometry.

Figure 2: a) The concentration profile of verification compound A as a function of particle radius [m] obtained numerically and analytically for a flat plate geometry using an irreversible first order reaction under isothermal conditions, using 100 equidistant grid cells. b) The concentration profile as a function of particle radius obtained numerically and analytically for a spherical geometry using an irreversible first order reaction under isothermal conditions, using 100 equidistant grid cells.

The error between the analytical and numerical profiles was defined as follows:

$$\epsilon = \max\left(\left|\frac{c_{numerical} - c_{analytical}}{c_{analytical}}\right|\right)$$

The maximum error was found to be < 1e^{-3} for both geometries when using 100 grid cells, indicating a high model accuracy and correct equation implementation for the isothermal case. To evaluate the non-isothermal case, representing the coupling of the mass and concentration balance using an Arrhenius law, the Weizs-Hicks solution is used. Within this approach, the coupled ODEs were transformed to a single ODE, which is solved using MATLAB's ode15s solver. The result is depicted in Figure 3.

In order to solve the Weisz-Hicks case two parameters are required: the Arrhenius number (β) and the Prater number (γ):

$$\beta = \frac{c_B\, \Delta H\, D_{eff}}{\lambda_{eff}\, T_B}$$

$$\gamma = \frac{E_{act}}{R\, T_B}$$

The latter represents the dimensionless heat of the reaction and the Arrhenius number expresses the sensitivity of the rate to temperature. These two dimensionless parameters are central to the Weisz and Hicks solution, allowing to describe the multiple steady states often found in mass and heat balances with Arrhenius coupling.

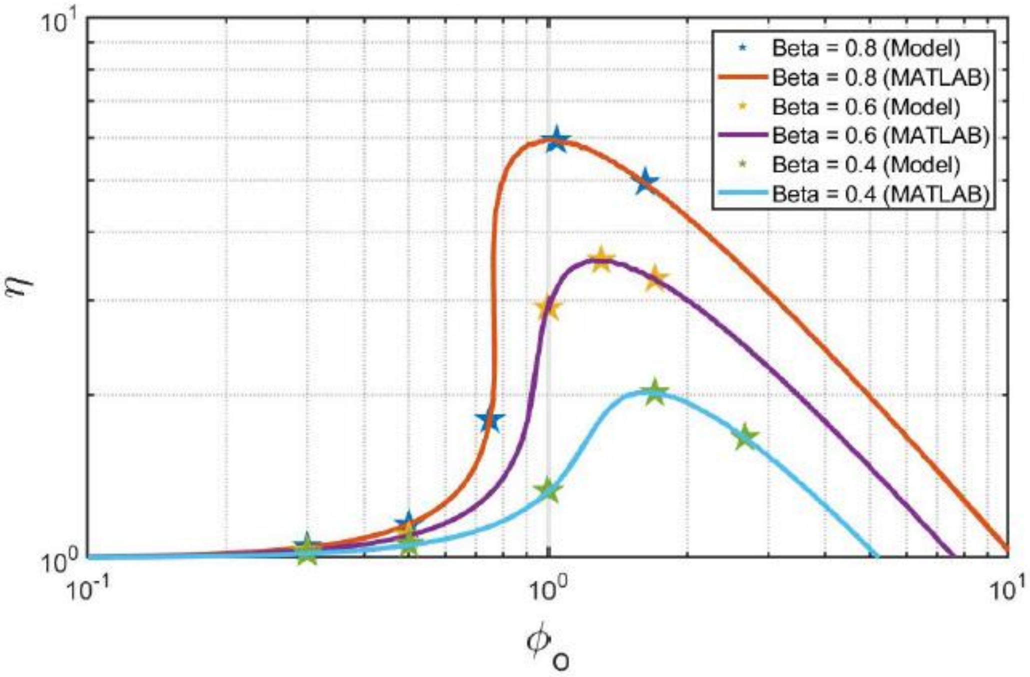

Figure 3: Comparison between Weisz & Hicks curves and numerically obtained model results for a model of 10, based on a spherical particle geometry.

In Figure 3, the multiple steady state curves of Weisz and Hicks (1995) and the numerical model results are shown for an Arrhenius number of 10, again using 100 grid cells. The error was again observed to be below 1e^{-3}, therefore confirming model accuracy and implementation.

The kinetic parameters of the CO_2 hydrogenation towards formic acid are described using a power law, with the temperature dependency implemented using an Arrhenius law. The rate constants are based on the work of Hensen *et al.* for a commonly employed gold catalyst, within this work triethylamine (NEt_3) is used as the trialkylamine extraction base. The produced formic acid is assumed to immediately bind to the available triethylamine, forming an adduct. Because of this very fast step, the total process is described using a single rate expression. In short the reaction can be summarized by:

$$x\,CO_2 + y\,H_2 + NEt_3 \rightleftarrows (\mathrm{y} \cdot \mathrm{FA} \cdot NEt_3)$$

Here, the forward rate is given by:

$$R_F = k_F\,[CO_2]^x\,[H_2]^y\,[NEt_3]$$

While the reverse reaction is given by:

$$R_R = k_R\,[y \cdot FA \cdot NEt_3]$$

The kinetic constants are described using an Arrhenius law, with the following kinetic parameters [7]:

Table 1 : Kinetic parameters of the catalytic hydrogenation of CO_2 to FA

Parameter	Forward reaction	Reverse reaction
E_{act} [J/mol]	5000	74000
Pre-exponential factor [1/s]	0.0052	$4.74 \cdot 10^{8}$
ΔH [kJ/mol]	-60.0	-167.0

The reaction enthalpy of the forward reaction was experimentally determined, while the reaction enthalpy of the backward reaction was estimated based on formation enthalpies taken from NIST.

Within the works of [5][9], it was also observed that small amounts of carbon-monoxide (CO) were present in the final product. The most probable cause is a reverse water-gas-shift (WGS) reaction, or decomposition of the produced formic acid. However, these small amounts of CO - a molar ratio of $5e^{-3}$ CO compared to the incorporated H2 [5][9] - were thus deemed insignificant resulting in 100% selectivity.

2.1.2 Particle-fluid interphase

Within the previous section Dirichlet boundary condition were used, meaning the concentration of any reagent and product at the edge of the catalytical concentration is equal to the bulk conditions. However, this assumption is often subject to the type of reactor used, as well as of the reaction conditions. For this reason, at the particle-fluid interphase, this assumption is often not valid. For this reason, the mass and heat transfer from the bulk fluid to the catalyst particle is modelled, allowing us to study the extent of external mass/heat transport resistance present allowing for an additional comparison between different reactor types.

According to film theory, the following relations can be used to describe the flux transport (J_i) of mass and heat between the bulk and particle phase, respectively:

$$J_i = k_{ext}\left(c_{i,b} - c_i|_{r=R}\right)$$

$$J_i = h_{ext}\left(T_{bulk} - T|_{r=R}\right)$$

Here, k_{ext} and h_{ext} are the external mass and heat transfer coefficients, both were obtained using appropriate correlations of previous works.

When applying the above equations to a particle model, the above equation can be enforced using the boundary conditions of the particle model. Here, the aforementioned Dirichlet boundary condition, in which the bulk concentration is imposed, is replaced by a Robin boundary condition, in which a flux is imposed. The flux boundary conditions for mass and heat are given by:

$$D_{eff,i}\left.\frac{\partial c_i}{\partial r}\right|_{r=R} = k_{ext}\left(c_{i,b} - c_i|_{r=R}\right)$$

$$\lambda_{eff}\left.\frac{\partial T}{\partial r}\right|_{r=R} = h_{ext}\left(T_B - T|_{r=R}\right)$$

The analytical expression used in Section 2.1.1. was adapted to the boundary condition discussed above, resulting in the following analytical expression for isothermal irreversible reaction for a spherical and flat plate geometry respectively:

$$\frac{c}{c_b} = \frac{\sinh(\lambda_c\,\varphi)}{\sinh(\varphi)} \cdot \frac{1}{\lambda_c} \cdot C_w$$

$$\frac{c}{c_b} = \frac{\cosh(\lambda_c\,\varphi)}{\cosh(\varphi)} \cdot C_w$$

Here, λ_c is the dimensionless particle coordinate, φ the Thiele modulus and C_w the drag coefficient given by:

$$\frac{1}{C_w} = \frac{\varphi \cdot \tanh(\varphi)}{Bi} + 1$$

$$Bi = \frac{k_{LS} \cdot L_c}{D_{eff}}$$

Within the above equations, k_{LS} is the external liquid-solid mass transfer coefficient and L_c the characteristic length of the corresponding geometry. The comparison of the obtained analytical and numerical results can be found in Figure 4, for a flat plate and spherical geometry using 100 grid cells. The error was again observed to be below $1e^{-3}$, therefore confirming model accuracy and implementation.

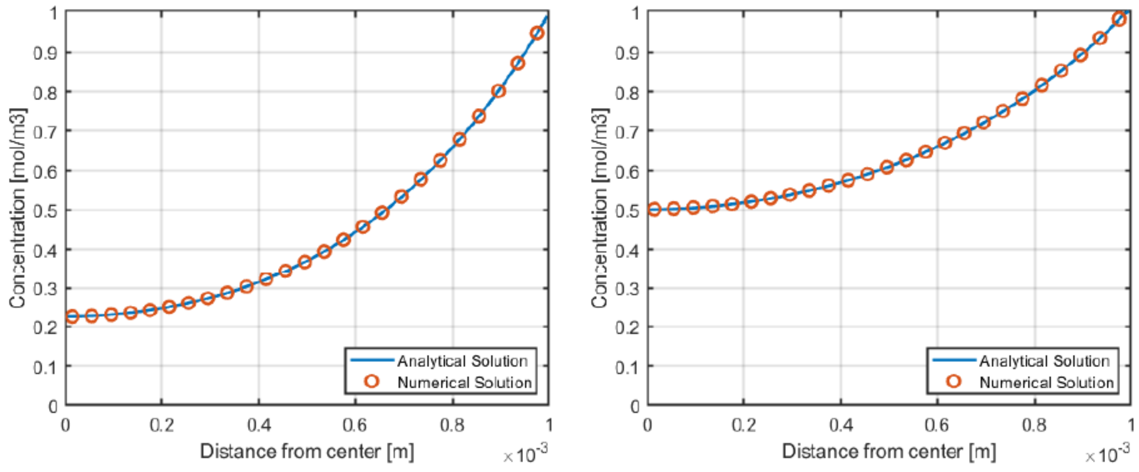

(a) Flat plate geometry.

(b) Spherical geometry.

Figure 4: a) The concentration profile as a function of particle radius obtained numerically and analytically for a flat plate geometry subject to Robin boundary conditions using an irreversible first order reaction under isothermal conditions, using 100 equidistant grid cells. b) The concentration profile as a function of particle radius obtained numerically and analytically for a spherical geometry subject to Robin boundary conditions using an irreversible first order reaction under isothermal conditions, using 100 equidistant grid cells.

2.1.3 Fixed bed reactor

Within the previous section the particle was connected to a bulk fluid while accounting for external transfer resistances. However, within the bulk fluid there is convective flow and in some cases axial dispersion. However, as stated before, axial dispersion is neglected by using L/dp ≥ 50 and a D/dp ≥ 25, respectively.

The following governing equation was used to design an upflow co-current fixed bed reactor:

$$\frac{\partial}{\partial z}(v\,c_i) = R_i$$

Here, *v* is the velocity of the phase (gas or liquid) for which the balance is used. It was opted to study a upflow co-current model as these flow configurations are known to have higher liquid-solid mass transfer rates and often higher liquid hold-ups compared to a downflow configuration.

The definition of the reactive term is dependent on the rigorous particle model in order to take external mass transfer into account, for a spherical particle the rate expression is given by:

$$R_i = D_{cat}(1 - \varepsilon_{bed})\,\frac{6}{d_{part}}\left(D_{eff,i}\,\frac{\partial c_i}{\partial r}\bigg|_{r=R}\right)$$

The governing equation for heat is analogous to the governing equation previously shown for mass. As is the case for the mass axial dispersion, heat axial dispersion is also neglected:

$$\frac{\partial}{\partial z}\left(v\sum_i (c_i \cdot C_{p,i})\;T\right) - \sum \Delta H_i\,R_i$$

Here, *Cp,i* is the heat capacity of component *i*. At the reactor inlet (x = 0), it was opted to enforce the concentration and temperature (Dirichlet boundary condition).

$$c_i|_{x=0} = c_{i,in}$$

$$T|_{x=0} = T_{i,in}$$

At the reactor outlet (x = L), the gradient in terms of mass and temperature should be equal to zero (Neumann boundary condition):

$$\frac{\partial c_i}{\partial z}\bigg|_{z=L} = 0$$

$$\frac{\partial T}{\partial z}\bigg|_{z=L} = 0$$

To allow for the derivation of analytical expressions, enabling the verification of the packed bed reactor model, two limiting verification cases were studied. Within the first case, the gas concentration was assumed to remain constant, while in the second case the liquid concentration was assumed constant. Additionally, as was done in the previous cases, an isothermal first order irreversible reaction was used, allowing for the usage of a Thiele modulus efficiency factor, leading to the following governing equation for the catalyst phase:

$$0 = -\eta \cdot k \cdot c_s + k_{ls} \cdot a_{LS} \cdot (c_L - c_s)$$

Using the above governing equation to obtain an expression for the solid concentration results in:

$$c_s = c_L \left(\frac{k_{ls} \cdot a_{LS}}{\eta \cdot k \cdot c_s + k_{ls} \cdot a_{LS}} \right)$$

Upon substituting the obtained expression for the catalyst phase concentration profile in the liquid phase balance:

$$\frac{\partial c_L}{\partial z} = A - c_L \cdot B$$

With:

A = $\left[\frac{\varepsilon_G \, k_{GL} \, a_{GL}}{v_L} \; c_G \right]$, and B = $\left[\frac{\varepsilon_G \, k_{GL} \, a_{GL}}{v_L} + \frac{\varepsilon_{void} \, k_{LS} \, a_{LS}}{v_L} - \frac{\varepsilon_{void} \, \varepsilon_{bed} \, k_{LS} \, a_{LS}}{v_L} \cdot \left(\frac{k_{ls} \cdot a_{LS}}{\eta \cdot k \cdot c_s + k_{ls} \cdot a_{LS}} \right) \right]$

Integration leads to the final verification expression for the limiting gas of constant gas concentration:

$$c_L = c_{L,0} \cdot \exp(-B \cdot z) - \frac{A}{B} \cdot \exp(-B \cdot z) + \frac{A}{B}$$

Within Figure 5, the analytical expression was compared to the numerical model results using 100 grid cells in the axial direction and 100 grid cells within the particle model. The maximal error obtained was $4.6e^{-6}$, similar results were obtained for the case of constant liquid concentration.

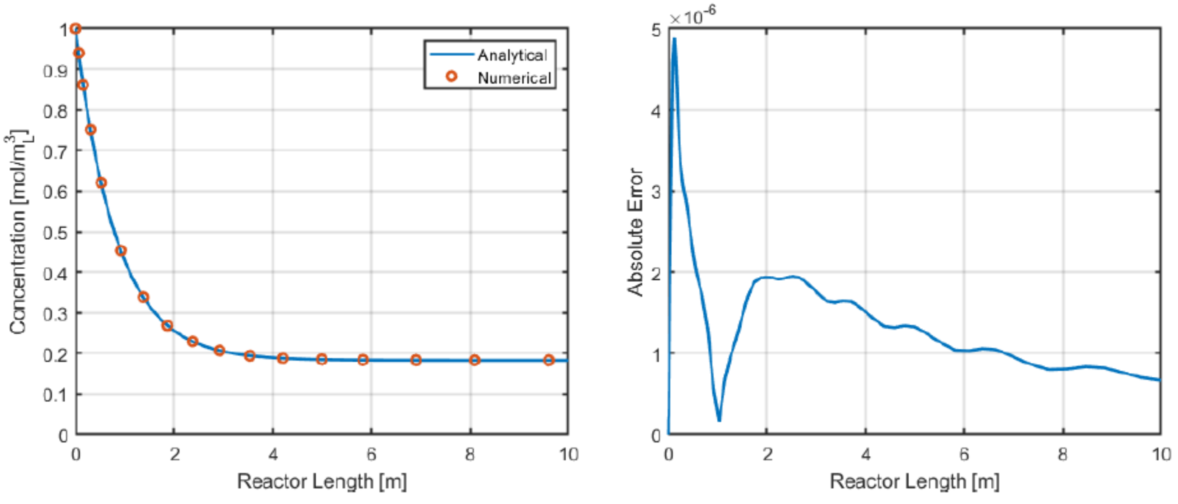

(a) Concentration profiles.

(b) Difference.

Figure 5: a) The concentration profile in the axial direction obtained analytically and numerically for an isothermal irreversible first order reaction, using 100 grid cells in the axial direction using spherical particles. b) The maximum error between the analytical expression and the numerical simulation

Within Section 2.1, the governing equations of the fixed bed reactor were discussed, including the kinetic rate expressions employed. The model implementation was verified using simplified analytical expressions.

2.2 Operating conditions and design parameters

The multiphase fixed bed reactor was designed by optimizing the operating conditions and the design parameters, with the goal of maximizing reactor performance. It was chosen to evaluate the reactor performance in terms of NEt_3 conversion and thus formic acid productivity:

$$X = \frac{c_{NEt_3,0} - c_{NEt_3}}{c_{NEt_3,0}}$$

Besides the triethylamine conversion, three criteria were studied to quantify the cause of performance limitations. The Weisz-Prater criterion for internal diffusion limitations (absent if < 1), the first Mears criterion for external diffusion limitations (absent if < 0.15) and the second Mears criterion for heat transfer (absent if < 0.15). These are given by, respectively:

$$C_{W,P,i} = \frac{r_1' \, \rho_{cat} R_{part}^2}{D_{eff,i} c_{i,s}} < 1$$

$$C_{M,i} = \frac{r_1' \, \rho_{bulk} R_{part} \, n}{k_{LS} c_{i,L}} < 0.15$$

$$C_{M,i} = \left| \frac{\Delta H_R r_1' \, \rho_{bulk} R_{part} \, E_{act}}{U_{cat} T^2 R} \right| < 0.15$$

Here, n is the reaction order, and U_{cat} the heat transfer coefficient and R the universal gas constant. As stated previously, the formation of FA from CO_2 and H_2 is 100 % selective, so no evaluation in terms of selectivity's and yields is required. An overview of the main operating conditions is given in Table 2.

Table 2 : Overview of the main operating conditions for the fixed bed reactor

Operating condition
Reactor inlet temperature, T_0^R (K)
Reactor zone pressure, P^R (bar)

The reactor inlet temperature was limited to 80°C to circumvent formic acid decomposition, while the pressure was limited to 72 bars. First the influence of these parameter was studied on a smaller scale reactor. Afterwards, the optimized reactor design is upscaled towards the desired production capacity of 200 kton/year.

First, the influence of the main operating conditions stated in Table 2 was studied, with results shown in Figure 6: Influence of operational pressure and temperature on the concentration at the reactor outlet, using the design parameters of Table 3Figure 6. To this end, the adduct concentrations at the end of the reactor were compared for different operational temperatures and pressures, with the other design parameters summarized in Table 3.

Table 3 : Design parameters used for the optimization of the main operating conditions in case of the fixed bed reactor

Reactor properties	Value
Reactor length, L (m)	10
Reactor inner diameter D_i (m)	0.1
Particle radius R_{part} (m)	0.001
Solid hold-up ε_s $(m_S^3\ /\ m_R^3\ )$	0.6
Catalyst loading L_D $(wt\%)$	1
Liquid velocity u_L $(m_L^3\ /\ m_R^2\ \ /\ s)$	9.22e^{-6}
Gas velocity u_G $(m_L^3\ /\ m_R^2\ \ /\ s)$	7.06e^{-6}

Here, it was found that the highest outlet concentration of the adduct is at the lowest temperature (40 degrees Celsius) and highest studied pressure, 72 bars. The latter is due to increased solubility due to higher gas activities.

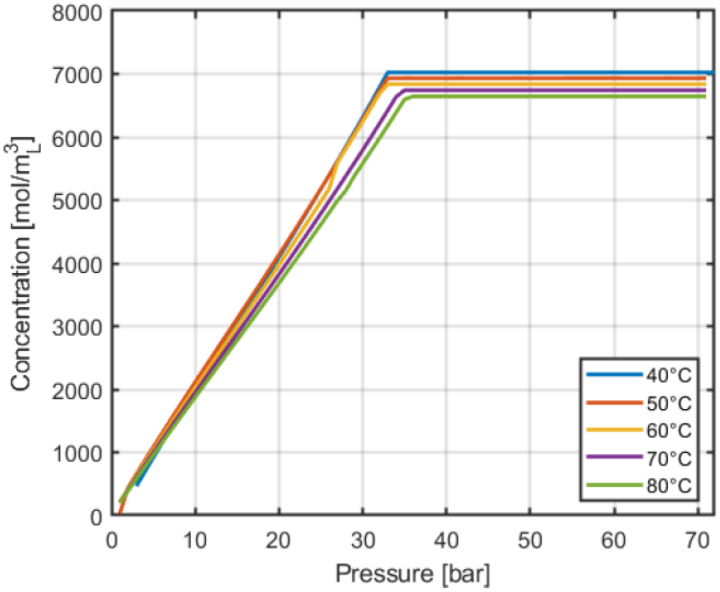

Figure 6: Influence of operational pressure and temperature on the concentration at the reactor outlet, using the design parameters of Table 3

To get a better understanding of the limitations in the above the reactor performance, the aforementioned criteria were used. From the Weisz-Prater criterion for internal diffusion limitations, strong intra-particle mass transfer limitations were found for all reagents and the adduct, which are most pronounced at lower temperatures due to lower diffusivity at lower temperature. A complete overview is presented within the appendix, while the most significant Figures of Merits are discussed within the next sections. It should be noted that all performance criteria were determined at the reactor outlet.

The internal effectiveness factor is discussed within Figure 7, here it was found that internal mass transfer limitations are present at lower temperatures.

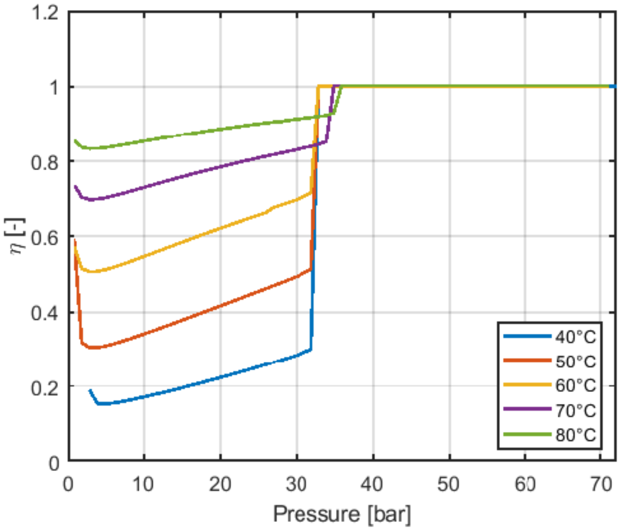

Figure 7: The internal effectiveness factor as function of operational pressures and temperatures, using the design parameters of Table 3. External mass transfer limitations can be assumed to be absent when $C_{M1,H2} < 0.15$

Besides internal diffusion limitations, external mass transfer limitations were found to be present for hydrogen at low operational pressures (<32 bar), and for triethylamine (> 32 bar), as depicted in Figure 8.

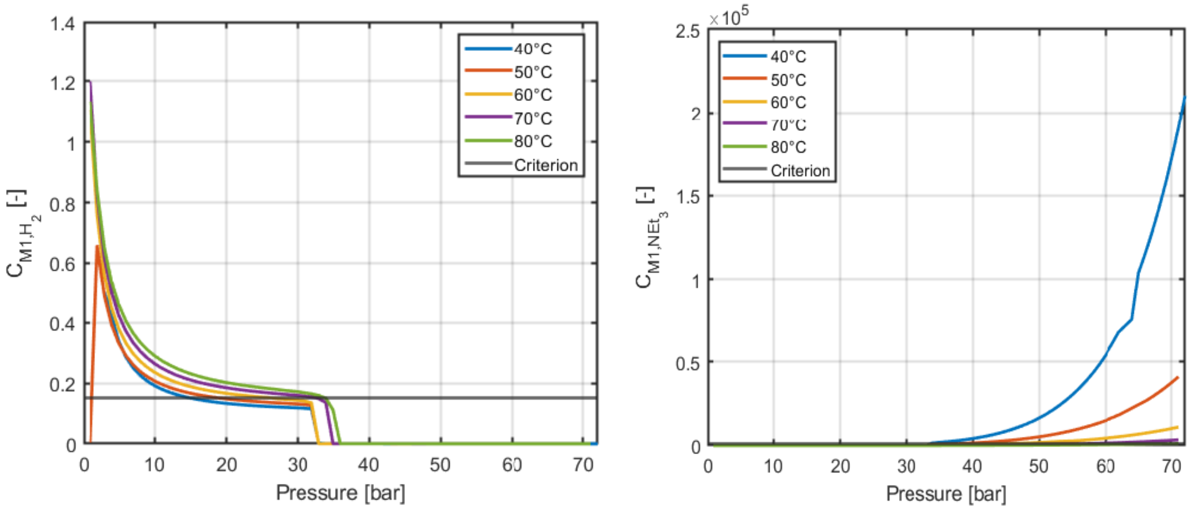

Figure 8: The first Mears criterion for hydrogen (right) and triethylamine (left) as function of operational pressures and temperatures, using the design parameters of Table 3. External mass transfer limitations can be assumed to be absent when CM1,H2 < 0.15

The temperature profile was found to remain constant over the reactor length, showing no thermal effects within the reactor. The absence of heat transfer limitations was also confirmed by the second Mears criterion, which was found to be $6.6e^{-9}$.

The optimal operational conditions in terms of productivity were established. Using the optimal operational conditions, the particle size and velocities were optimized to circumvent the internal and external mass transfer limitations as much as possible, depicted in Figure 9 and Figure 10 . All other design parameters were kept constant as given in Table 3.

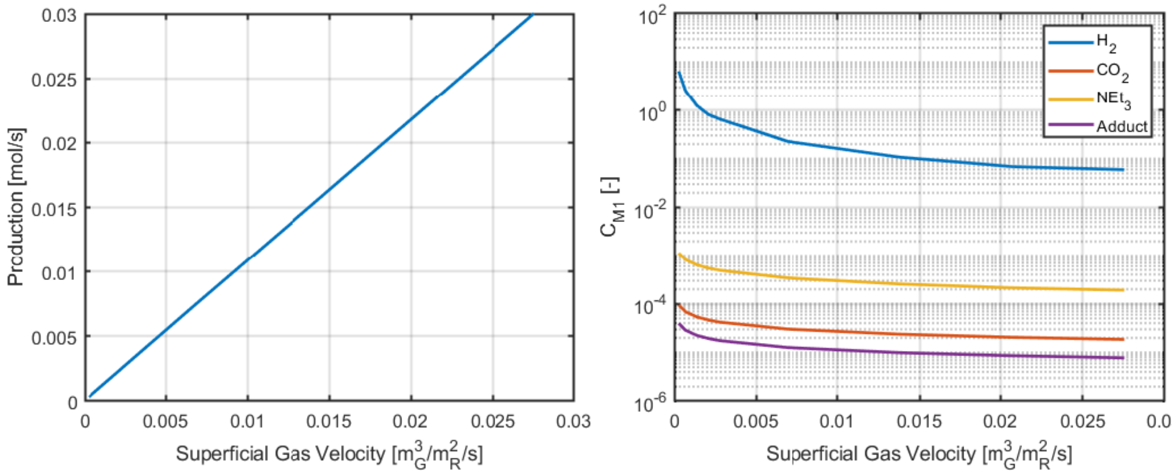

(a) Production Profile (b) 1^{st} Mears Criterion.

Figure 9: Optimization of the catalyst particle size at the determined optimal operational conditions. a) Adduct concentration at the reactor outlet. b). Weisz-Prater crition to quantifiy the extent of intra-particle diffusion limitations (absent < 1)

The Weizs-Prater criterion was found to remain above 1 for all components at all particle radii, indicating the presence of intra-particle diffusion limitations. The ratio of the liquid velocity to the gas velocity was kept constant. Here, it was found that at gas velocities above 0.01, external mass transfer limitations are overcome for all components.

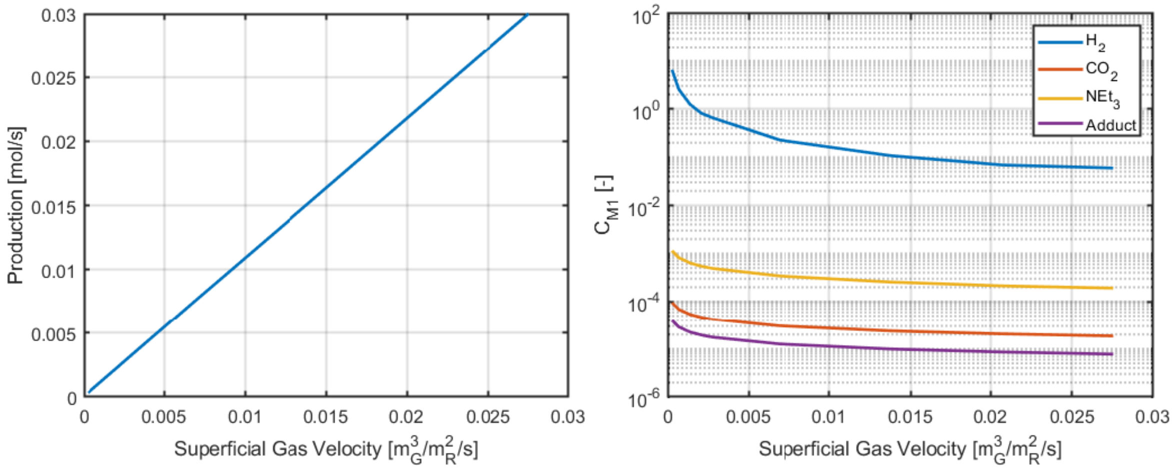

(a) Production Profile (b) 1^{st} Mears Criterion.

Figure 10: Optimization of the gas and liquid velocities at the determined optimal operational conditions. a) Adduct production rate. b). First Mears crition to quantifiy the extent of external mass transfer limitations (absent if < 0.15)

Within Section 2.3, the optimal operational and design parameters for the fixed bed reactor were determined. To this end, a small scale reactor was used in an up-flow co-current configuration. Criteria were used to estimate the extent of the most common mass transfer resistances (external and internal), and the influence of temperature profiles. Here, it was found that the optimized design is only suffering from mass transfer limitations for hydrogen, while the temperature profiles were found to be negligible for both the column as well as the particle.

2.3 Reactor scale up

The fixed bed reactor optimal operating conditions were based on maximal formic acid productivity within the previous section. These results were obtained by running simulations on a smaller scale reactor, which allowed a simpler analysis of the effect of such conditions on the reactor performance. Thereafter, the design can be scaled-up for the desired production rate of 200 kton/year. From a literature study it was found that these types of reactors in general have heights between 6 and 10 meters and a height over diameter ratio between 5 and 7 [14,15], which was thus taken as the maximum reactor size. The particle size was taken as 1 mm, and the H/D ratio as 5. **Erreur ! Source du renvoi introuvable.**Figure 11 shows the formic acid productivity per reactor volume for several residence times, as well as the productivity normalized per catalyst weight.

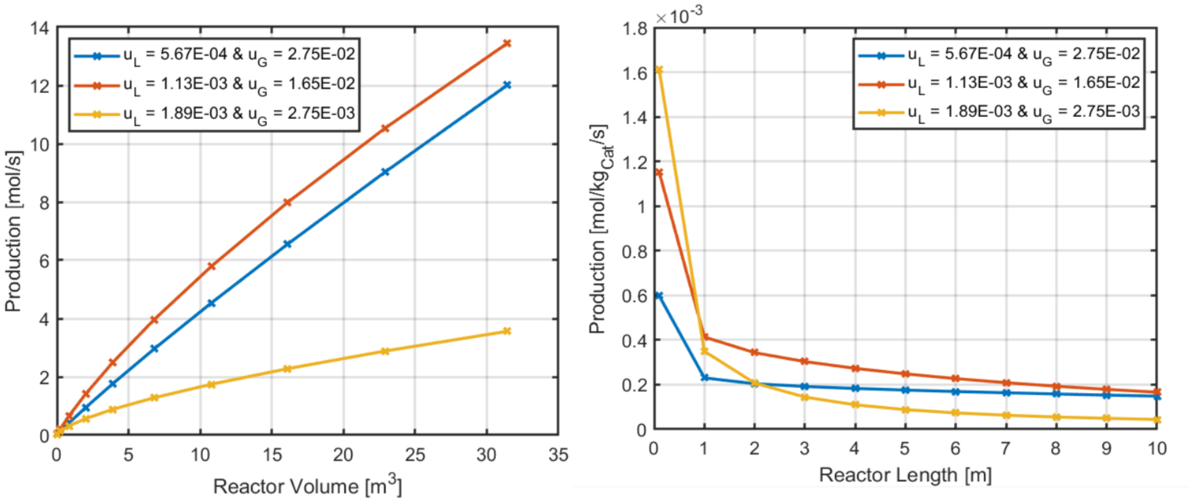

*Figure 11: left) The production of the co-current upflow packed bed reactor versus reactor volume for three different superficial velocities using the optimized operational and design parameters summarized in**Erreur ! Source du renvoi introuvable.**. Right) The formic acid productivity presented left) normalized per catalyst mass*

Based on these results, it was concluded that the targeted production of 200 kton/year requires 7 reactors of 10 meters high and 2 meters wide.

3 Section 2 – Rotor-stator Spinning-Disc Reactor modelling (rs-SDR) and parameter optimization

A schematic representation of the rotor-stator Spinning Disc Reactor (rs-SDR) is sketched in Figure 12. The rs-SDR consists out of rotating disc, called the rotor, which is surrounded by a cylindrical housing called the stator. The axial gap between the rotor and the stator is often in the order of 1 mm [16,17]. The combination of high sheer conditions and short diffusional lengths results in an increase mass transfer performance compared to conventional equipment such as the fixed bed reactor discussed previously, motivating the study into such intensified equipment after significant liquid-solid mass transfer limitations were found in Section 1 for fixed bed reactors.

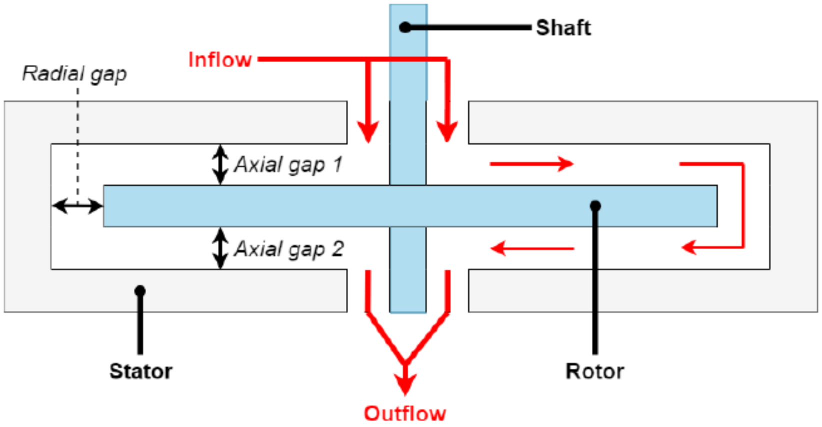

Figure 12: Schematic representation of the rs-SDR.

Rotational velocities can readily reach up to 4000 rpm, therefore giving rise to a high degree of turbulence and thus fast renewal of liquid at both the gas-liquid as well as the liquid-solid interfaces [16]. Such degrees of turbulence are preferable as turbulence can enhance mass, momentum and energy transport, resulting in improved mass transfer characteristics. The small axial gap design generates a high shear force on the fluid phase resulting in further enhancements of the aforementioned high turbulence rates. Beside turbulent behaviors, the small geometry of the axial gap also leads to early bubble pinch-off in multiphase flows, which in turn results in a larges gas interfacial area due to smaller bubbles. These combined characteristics give rise to high mass transfer rates for gas-liquid, liquid-solid and liquid-liquid flows [16,17].

For multiphase systems the rs-SDR can be operated in two modes: counter current and co-current feeding. Within the counter current configuration, the liquid is fed from the top of the reactor while the gas is fed from the bottom and vice versa in the co-current strategy. Previous works such as the work of de Beer *et al.* [17] have shown that the co-current feeding allows larger gas hold-ups, prompting larger interfacial areas. It was thus opted to model a co-current feeding strategy as previous sections revealed limited solubility of the reacting gasses in triethylamine.

The catalytic phase was incorporated into the reactor through the usage of a slurry catalyst such as in the work of Chauduri *et al.*

3.1 Modelling approach and governing equations

Within Section 1, the modelling strategy of the fixed bed reactor was discussed. This model consisted of versatile building blocks used to describe the different length scales present in a macroscopic catalytic reactor. Within the rs-SDR model, the building blocks of the particle and the particle-liquid interphase were employed again. For this reason, they are not discussed and no verification is shown within this section of the report. The assumptions made within the fixed bed reactor model, were also used within the rs-SDR study.

Previous experimental work by Meeuwse *et al.* [18] has shown that the phenomenological modelling approach of a multiphase is dependent on the position within the reactor. On top of the rotor, meaning at the reactor inlet, a thin liquid film is present with the gas flowing over thin film, hence this region is known as the film flow region (FFR). Below the disc and in the radial gaps between the disc and the stator, the gas phase is dispersed in the liquid phase, therefore this region is often referred to as the dispersed flow region (DFR). Experimental works such as [18] have shown that the liquid phase in the FFR shows plug flow behaviour, while the gas phase acts similar to an ideally stirred tank (CSTR). These flow behaviours are opposite in the DFR. Within Figure 13, a summary of the modelling strategy of each of these regions is presented.

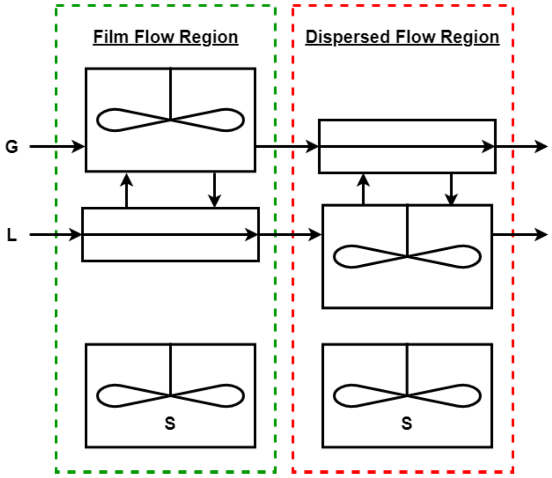

Figure 13: Graphical representation of the modelling strategy for a multiphase single stage rs-SDR, based on the work of Meeuwse et al. [18].

3.1.1 Modelling approach and governing equations within the film flow region

Within the multiphase 1D-phenomenological model the film flow region (FFR), indicated by the F index, the liquid is modelled using ideal plug behavior, while the gas is modelled as an ideally stirred tank reactor (CSTR). Similarly to the packed bed model, the solid phase was modelled using the particle model and particle-fluid interface described in Section 1. The governing equation for the gas and liquid balance are given by:

$$\frac{\partial c_{G,F}}{dt} = \frac{\varphi_g}{V_{G,F}}\left(c_{G,F,0} - c_{G,F}\right) - \frac{1}{\varepsilon_{G,F}}\left(k_{GL}a_{GL}\right)_F \cdot \left(c_{G,F} - c_{L,F}\right)$$

$$\frac{\partial c_{L,F}}{dt} = -\varphi_L \cdot \frac{\partial c_{L,F}}{\partial V_{R,F}} + \left(k_{GL}a_{GL}\right)_F \cdot \left(c_{G,F} - c_{L,F}\right) - \left(k_{LS}a_{LS}\right)_F \cdot \varepsilon_{part} \cdot \left(c_{L,F} - c_{S,F}\right)$$

Here, $V_{R,F}$ represents the reactor within the FFR, φ_i the volumetric flowrate of phase i, $\varepsilon_{G,F}$ the gas-hold up in the FFR and ε_{part} the void fraction of the catalyst.

In order to numerically solve the Partial Differential Equation (PDE) governing the liquid phase, a method of lines was employed to transform the PDE into an ODE. To this end, the derivative towards the reactor volume was rewritten into a series of CSTRs, as an infinite amount of CSTRs would result in ideal PFR behavior. An illustration of the tanks-in-series approach is depicted in Figure 14.

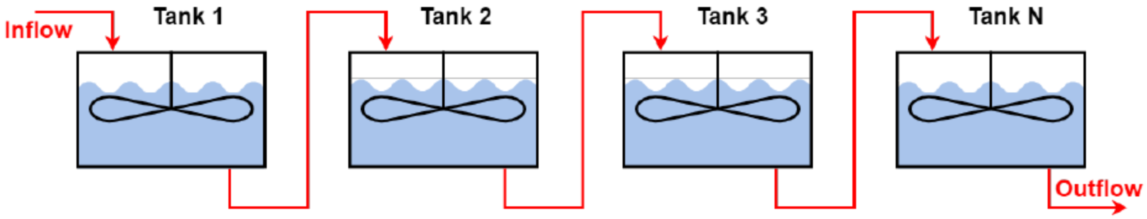

Figure 14: Schematic representation of N CSTR's for the tank-in-series approach.

The amount of tanks required for the mathematical transformation was calculated using the relation between the energy dissipation and the Peclet number [19]. Due to the close relation between mass and heat characteristics, the heat model strategy was taken analogous to mass.

The numerical implementation of the tanks-in-series model was subjected to extensive verification by derivation of an analytical expression for the individual tanks used to model the liquid phase. The approach taken is closely related to the approach taken within Section 2.1.3, where the position derivative used with the fixed bed reactor is substituted by the time derivative of the rs-SDR simulations. The obtained analytical expression is given by:

$$c_{L,F} = c_{L,F,0} \cdot \exp(-B \cdot t) - \frac{A}{B} \cdot \exp(-B \cdot t) + \frac{A}{B}$$

with A and B being defined as:

$$A = \frac{\varphi_L}{V_{L,F}} \cdot c_{L,F,0} + \frac{(k_{GL} a_{GL} \varepsilon_G)_F}{\varepsilon_{L,F}} \cdot c_{G,F}$$

$$B = \frac{\varphi_L}{V_{L,F}} + \frac{(k_{GL} a_{GL} \varepsilon_G)_F}{\varepsilon_{L,F}} + \frac{(k_{LS} a_{LS}\ \varepsilon_s\ \varepsilon_{void})_F}{\varepsilon_{L,F}} - \frac{(k_{LS} a_{LS}\ \varepsilon_s\ \varepsilon_{void})_F}{\varepsilon_{L,F}} \cdot \left(\frac{(k_{LS} a_{LS})_F}{\eta k_1 + (k_{LS} a_{LS})_F}\right)$$

A comparison between the analytical solution and the numerical model is shown in Figure 15, with the largest absolute error found to be $8.1e^{-4}$.

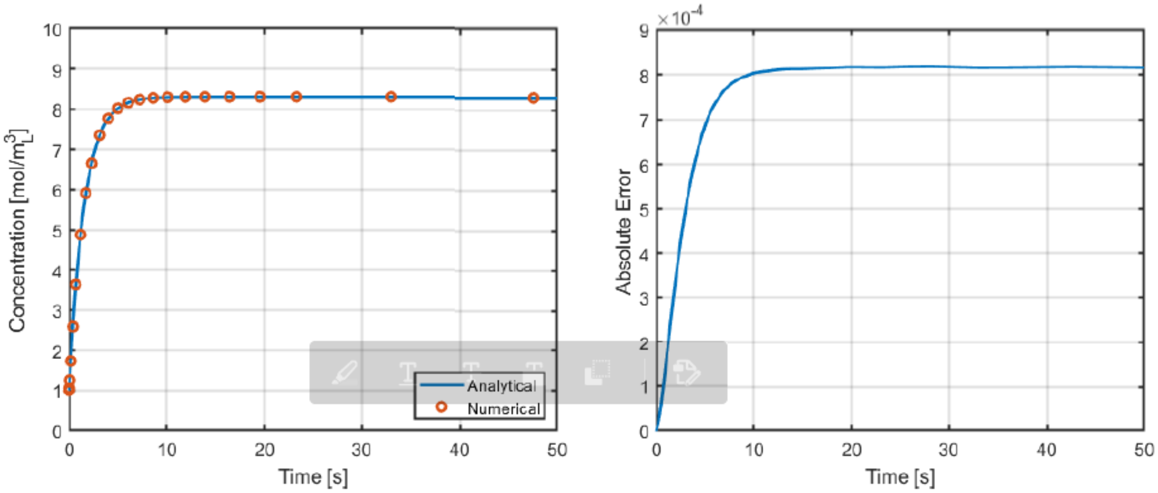

(a) Concentration profiles.

(b) Difference.

Figure 15: Verification of the liquid phase tanks-in-series model for the FFR. 100 grid cells were used.

Similarly, the numerical implementation of the gas-phase CSTR balance was verified. The derived analytical expression is given by:

$$c_{G,F} = c_{G,F,0} \cdot \exp(-B \cdot t) - \frac{A}{B} \cdot \exp(-B \cdot t) + \frac{A}{B}$$

with A and B given by:

$$A = \frac{\varphi_G}{V_{G,F}} c_{G,F,0} + (k_{GL} a_{GL})_F\ c_{L,F}$$

$$B = \frac{\varphi_G}{V_{G,F}} + (k_{GL} a_{GL})_F$$

The rewritten form of above equation is compared to obtained numerical solutions in Figure 16. From here, it is again found that the numerical solutions closely resemble the analytical one, with maximum error of $3.3e^{-5}$.

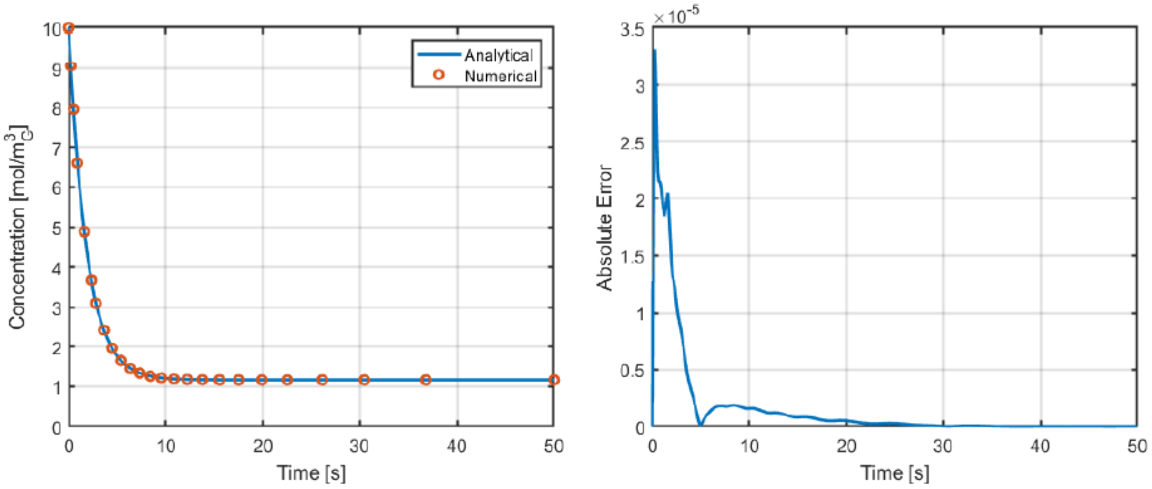

(a) Concentration profiles.

(b) Difference.

Figure 16: Verification of the gas phase CSTR model for the FFR. 100 grid cells were used.

3.1.2 Modelling approach and governing equations within the dispersed flow region

Within the multiphase 1D-phenomenological model the dispersed flow region (DFR), indicated by the D index, the gas is modelled using ideal plug behavior, while the liquid is modelled as an ideally stirred tank reactor (CSTR), as was summarized in Figure 13. The governing equations for the gas and liquid are as follows:

$$\varphi_G \cdot \frac{\partial c_{G,D}}{\partial V_{G,D}} = -(k_{GL}a_{GL})_F \cdot (c_{G,F} - c_{L,F})$$

$$\frac{\partial c_{L,D}}{dt} = \frac{\varphi_L}{V_{L,D}} \cdot (c_{L,D,0} - c_{L,D}) + \left(\frac{k_{GL}a_{GL}}{\varepsilon_L}\right)_D \cdot (c_{G,D} - c_{L,D}) - \left(k_{LS}a_{LS} \cdot \frac{\varepsilon_{part}}{\varepsilon_L}\right)_D \cdot (c_{L,D} - c_{S,D})$$

Similarly to the film flow region, the gas phase PFR was modelled using a Tanks-in-Series approach. The verification strategy used within the FFR was thus also employed for the DFR, with a reversal of the gas and liquid approaches presented in Section 3.1.1. A maximum absolute error of 3.3e^{-5} was found for the gas phase implementation, while a maximum absolute error of 2.3e^{-3} was found for the liquid phase implementation.

Within Section 3.1, the governing equations of the rotor-stator Spinning Disc Reactor (rs-SDR) were presented. Here, the catalyst is incorporated using a slurry approach. The model implementation was verified using simplified analytical expressions.

3.2 Operating conditions and design parameters

The optimal operational conditions given in Table 2 were studied for the rs-SDR. Based on the work of Chaudhuri *et al.* (2021) the catalyst weight percentage was set at 20wt% [20], and was assumed constant during the study. The design parameters are given in Table 4.

Table 4 : Design parameters used for the optimization of the main operating conditions in case of the rs-SDR using 10 tanks

Reactor properties	Value
Rotor diameter, $r_D\,(m)$	0.125
Rotor connection diameter, $r_x\,(m)$	0.0125
Rotor- stator gap x-direction, $r_y\,(m)$	5.0e^{-3}
Rotor-stator gap y-direction, $h\,(m)$	1.0e^{-3}
Rotor thickness, $t_d\,(m)$	3.0e^{-3}
Particle radius $R_{part}\,(m)$	200.0e^{-6}
Solid hold-up $\varepsilon_s\,(m_s^3\,/\,m_R^3)$	0.0727
Catalyst loading $L_D\,(wt\%)$	1
Liquid flowrate $\varphi_L\,(m_L^3\,/\,s)$	6.11e^{-6}
Gas flowrate $\varphi_G\,(m_G^3\,/\,s)$	6.11e^{-6}
Rotational speed $\omega\,(rad\,/\,s)$	100

The effect of temperature and pressure on the resulting adduct concentrations are shown for both the film flow region (FFR) and the dispersed flow region (DFR) in Figure 17. Here, it was found that the highest outlet concentration of the adduct is at the lowest temperature (40°C) and highest studied pressure, 72 bars. The latter is due to increased solubility due to higher gas activities.

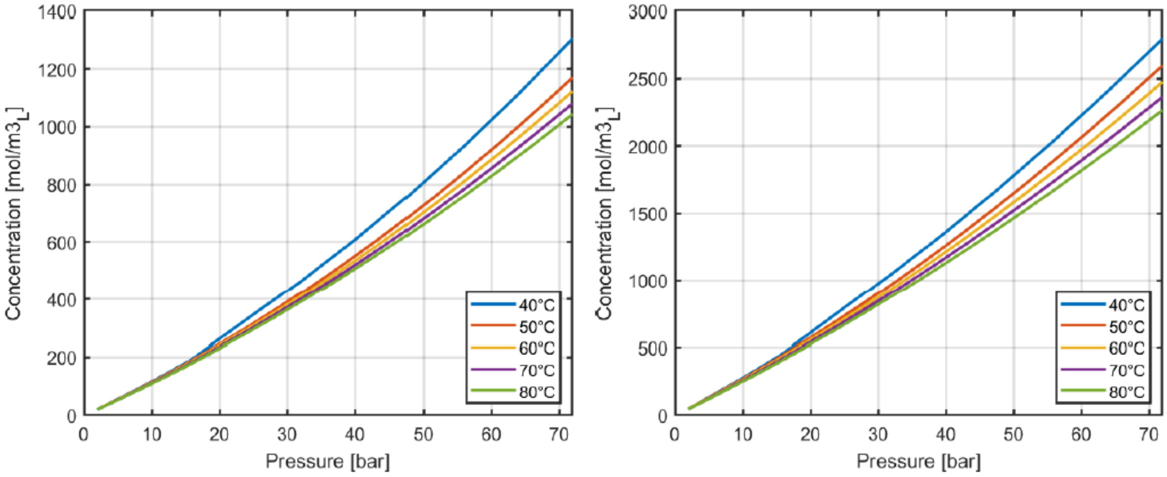

(a) FFR (b) DFR

*Figure 17: Pressure and temperature effect on the concentration at the end of both the FFR and DFR region with a catalyst in the slurry phase, using parameters from Table 4**Erreur ! Source du renvoi introuvable.***

At the optimal operational conditions, 72 bar and 40°C, the ratio between the gas and liquid flow rate was optimized based on concentration and productivity at the reactor outlet, depicted in Figure 18. Within Figure 18, a clear optimum is found at a production capacity of 0.02 mol/s at a gas to liquid flowrate ratio of 0.4.

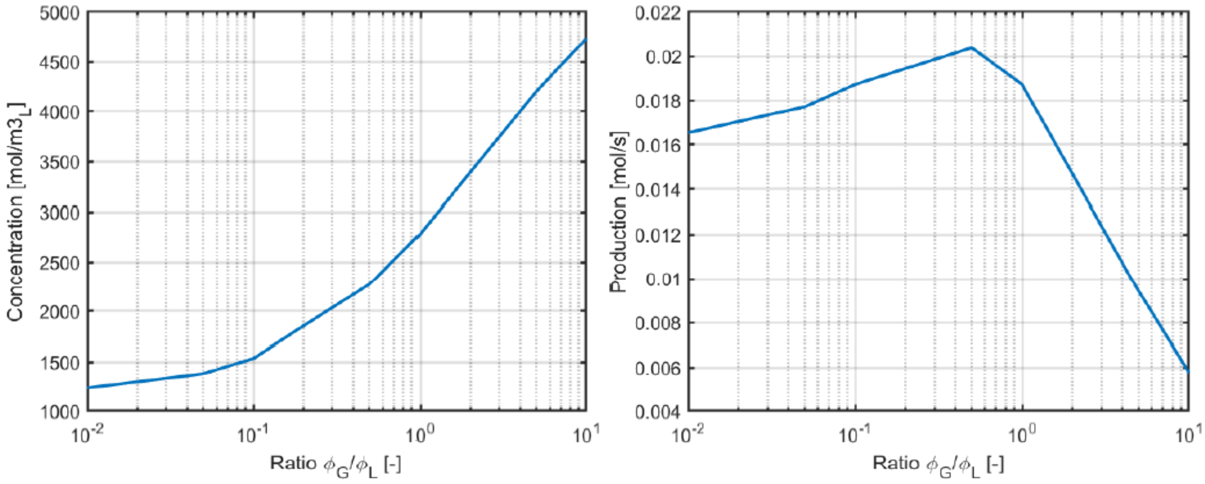

(a) Concentration (b) Production

Figure 18: Optimization of gas to liquid flow rate. Left) Influence on the adduct outlet concentration. Right) Influence on formic acid productivity.

Lastly, the rotational speed was optimized, with the results illustrated in Figure 19. Here, it was found that an increase in rotational speed leads to an increase in formic acid concentration due to a decrease of external mass transfer limitations.

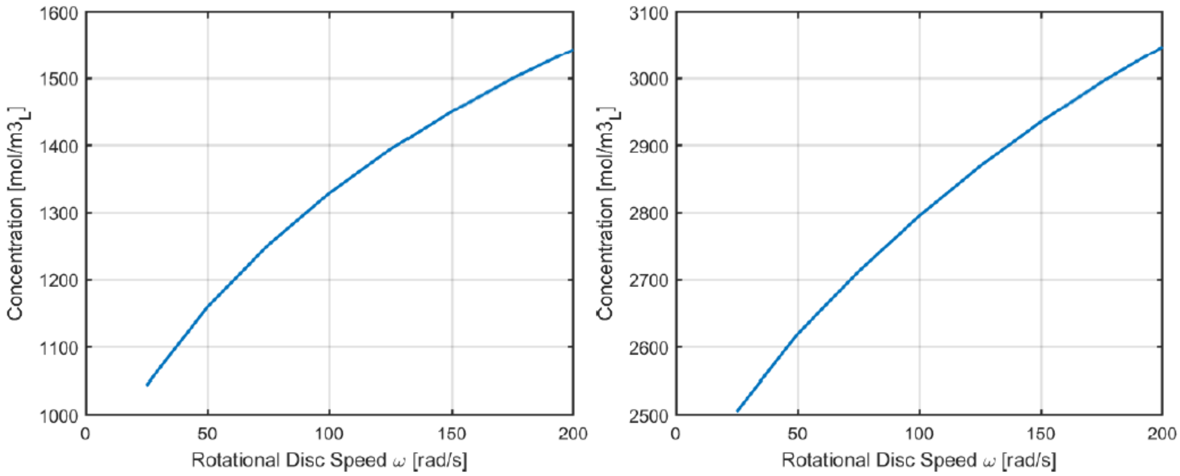

(a) FFR (b) DFR

Figure 19: Optimization of the rotational speed. Left) Influence on the adduct outlet concentration at the end of the FFR. Right) Influence on the adduct outlet concentration at the end of the DFR.

Within Section 3.2, the optimal operational and design parameters for the rs-SDR were determined. To this end, a small scale reactor was used. At the optimal operational conditions, 72 bar and 40°C, the ratio between the gas and liquid flow rate was optimized based on concentration and productivity at the reactor outlet. A clear optimum is found at a production capacity of 0.02 mol/s at a gas to liquid flowrate ratio of 0.4.

3.3 Reactor scale up

The results discussed within the previous section were obtained by running simulations on a smaller scale reactor, which allowed a much simpler analysis of the effect of such conditions on the reactor performance. Thereafter, the design can be scaled-up for the desired production rate of 200 kton/year. To this end, several rotor radii and rs-SDRs in series were tested, with production capacity and conversion depicted in Figure 20.

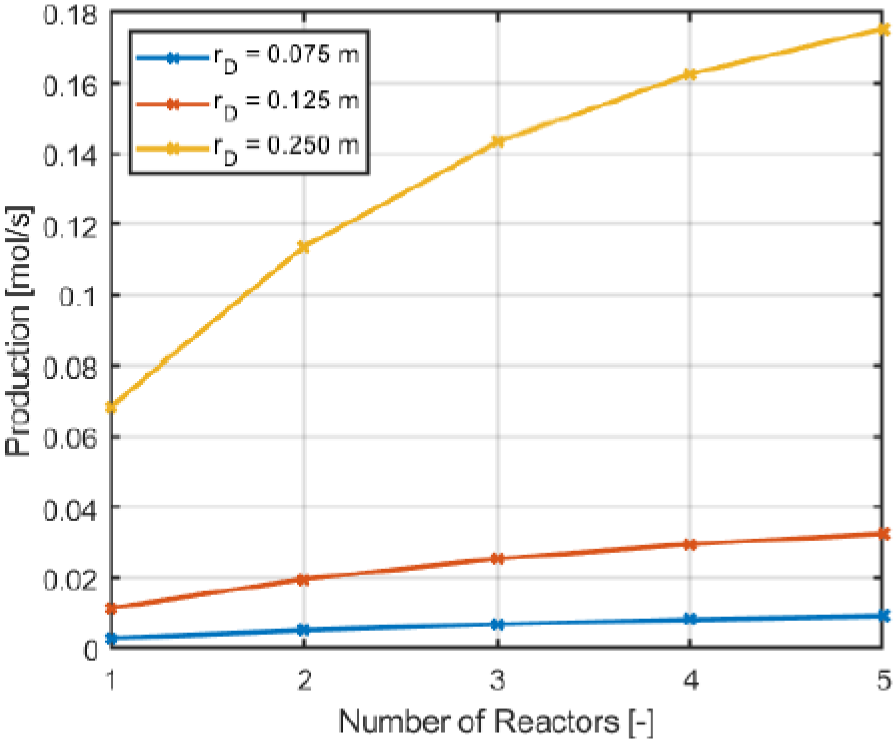

Figure 20: The effect of the disc radius and the number of rs-SDRs stages in series in terms of formic acid production (left)

Based on Figure 20, it was opted to use a disc radius of 25 cm, which corresponds to a reactor volume 1.1722e-04 m^3 of per stage. Using a conversion of 62% at the optimal operational and design parameters, the required production capacity would require the usage of 638 stages.

Based on these results, it was concluded that the targeted production of 200 kton/year requires 638 reactor stages, with an CO_2 conversion of 62 percent.

4 Comparison of reactor types

Lastly, the two reactor types were compared in terms of formic acid productivity per catalyst mass at an equal residence time of 8 seconds, with the results depicted in Figure 21. Here, the design of the packed bed reactor is equal to that of the optimal conditions discussed in Section 2, but with increased gas and liquid superficial velocities to decrease the residence time to 8 seconds. The number of reactors corresponds to sequential reactors in case of the packed bed reactor, and stages in case of the rs-SDR.

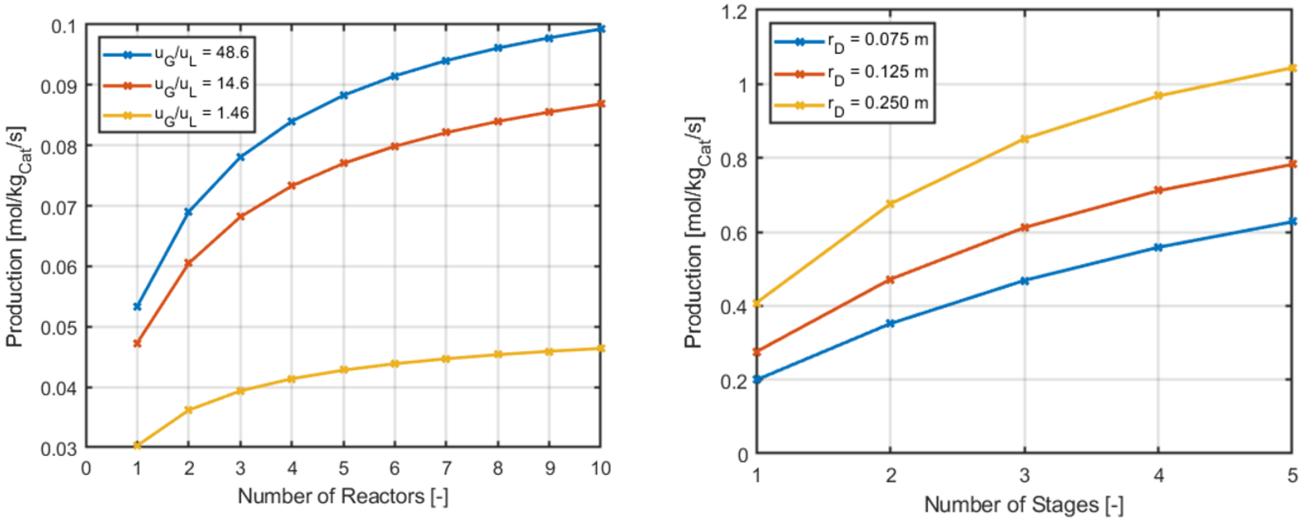

Figure 21: The formic acid productivity per kg of catalyst at equal residence time for the packed bed (left) and rs-SDR (right)

From Figure 21 it can be found that the productivity normalized per kg of catalyst at equal residence time is higher for the rs-SDR, due to the circumvention of external mass transfer resistances. Within **Deliverable 4.3B**, experimental model validation of the existence or absence of such resistances will be shown.

However, only a small quantity of catalyst can be incorporated into such a reactor. In order to normalize per reactor volume, the productivity per kg of catalyst has to be multiplied by the solid hold-up. For an upflow co-current fixed bed reactor, the solid hold up is typically in the order of 0.6 $m^3_{catalyst}$ / $m^3_{reactor}$, while for a rs-SDR using a slurry approach (meaning the catalyst is pumped with the liquid) only 0.0727 $m^3_{catalyst}$ / $m^3_{reactor}$ can be accomplished, based on the work of Chaudhuri *et al* [20]. The productivity per reactor volume is compared for the most optimal design using 5 stages, so in case of the packed bed reactor at a u_g/u_l of 48.6 and in case of the rs-SDR for a disc radius of 0.250 meter. This translates to a productivity per $m^3_{reactor}$ per second of 0,065 moles of FA for the fixed bed reactor, and 0,071 moles of FA for the spinning disc reactor**, i.e. same order values of productivity.** From this side, the advantage of the spinning disc reactor over the fixed bed reactor is not clearly evidenced.

Besides, the usage of the rs-SDR will require the usage of multistage equipment, as can be found from Figure 21. According to Meeuwse *et al.* [19] such reactors require more sophisticated equipment than conventional reactors, such as the fixed bed reactor designed within this Deliverable. This translates to **higher equipment costs, higher**

risk of mechanical failure due to the rotating parts. Even though such equipment is widely used, such as compressors, they are known for their **higher maintenance costs**. Besides this, rs-SDRs have a high energy dissipation rate leading to an increased energy input. Therefore, according to Meeuwse *et al.,* the switch of conventional equipment to intensified equipment such as the rs-SDR, is only economically attractive when the high heat and mass transfer rates justify the significant increase in investment (CAPEX) and operational costs (OPEX).

As could readily be seen within sections 2 and 3, the kinetics of the hydrogenation of CO_2 to formic acid are on the slow side, with the most optimal residence times in the order of magnitude of hours when using the one of the most active catalysts described within literature, namely Au/Al_2O_3. Such residence times are often an indication of kinetic limitations. This indication was also found when looking at the productivity rates of around 0,065 mol FA per $m^3_{reactor}$ per second for the packed bed reactor, while the rs-SDR only leads to a performance increase of 0,007 moles of FA per second. **Such a productivity increase is most likely not sufficient to make the rs-SDR economically attractive**. A techno-economic evaluation will be shown in **Deliverable 4.3B** and in the techno-economic analysis planned in **Deliverable 6.3**

5 Conclusions and perspectives

In this report, a fixed bed reactor and a rs-SDR were designed for a desired production capacity of 200 kton/year, based on the hydrogenation of CO_2 to formic acid using a Au/Al_2O_3 catalyst and triethylamine as an extraction base. To this end, 1D-phenomenological reactor models were developed, the operational and design parameters optimized and finally the reactors enabling a formic acid production of 200 kton/year. Both models make use of modelling technique known as non-isothermal heterogeneous reactor modelling. Here, the particle and the fluid phases are modelled separately, allowing for examination of the profiles in terms of concentration and temperature within in catalyst particles as well as within the fluid phase.

The design for the **fixed bed reactor** corresponds to an up-flow co-current configuration, which was selected due to its high mass transfer rates compared to a downflow configuration. First, the governing equations of the fixed-bed reactor were presented, after which several verification cases were presented using simplified kinetics to allow for analytical expressions. The models were found to be highly accurate, with a maximum error below $1e^{-6}$. The design and operational parameters were optimized using a smaller reactor, after which the reactor was up-scaled to allow for the desired productivity. In order to evaluate the existence of mass transfer resistances several well-known criteria were employed. Here, it was found that the optimized design is only suffering from mass transfer limitations for hydrogen, while the temperature profiles were found to be negligible for both the column as well as the particle. **Based on these results, it was concluded that the targeted production of 200 kton/year requires 7 reactors of 10 meters high and 2 meters wide.**

As was the case for the fixed bed reactor, **for the spinning disc reactor** the governing equations were discussed first after which several verification cases were presented using simplified kinetics to allow for analytical expressions. The models were again shown to be highly accurate with errors in the order of 1e-6. Within Section 3.2, the optimal operational and design parameters for the rs-SDR were determined. As was the case for the fixed bed reactor, a small-scale reactor was used. At the optimal operational conditions, 72 bar and 40°C, the ratio between the gas and liquid flow rate was optimized based on concentration and productivity at the reactor outlet. A clear optimum is found at a production capacity of 0.02 mol/s at a gas to liquid flowrate ratio of 0.4. **Based on this design, it was concluded that the targeted production of 200 kton/year requires 638 reactor stages, with an CO_2 conversion of 62 percent.**

As underlined earlier, according to Meeuwse *et al.,* the switch of conventional equipment, such as packed bed reactor, to intensified equipment, such as the rs-SDR, is only economically attractive when the high heat and mass transfer rates justify the significant increase in investment (CAPEX) and operational costs (OPEX), which is clearly not the case here, the productivity rates of the packed bed reactor being around 0,065 mol FA per $m^3_{reactor}$ per second, while the rs-SDR only leading to a performance increase of 0,007 moles of FA per second. **Such a productivity increase is most likely not sufficient to make the rs-SDR economically attractive.**

Within the following months, the separation process will be developed using Aspen Plus V11. Besides the design of the operation train, the model will be experimentally validated.

6 Bibliography

1. Álvarez, A. *et al.* Challenges in the Greener Production of Formates/Formic Acid, Methanol, and DME by Heterogeneously Catalyzed CO2 Hydrogenation Processes. *Chem. Rev.* **117**, 9804–9838 (2017).
2. Hietala, J. *et al.* Formic Acid. in *Ullmann's Encyclopedia of Industrial Chemistry* **1**, 1–22 (Wiley-VCH Verlag GmbH & Co. KGaA, 2016).
3. Putten, R. Van, Wissink, T., Swinkels, T. & Pidko, E. A. ScienceDirect Fuelling the hydrogen economy : Scale-up of an integrated formic acid-to-power system. *Int. J. Hydrogen Energy* 1–9 (2019). doi:10.1016/j.ijhydene.2019.01.153
4. Bulushev, D. A. & Ross, J. R. H. Heterogeneous catalysts for hydrogenation of CO2 and bicarbonates to formic acid and formates. *Catal. Rev. - Sci. Eng.* **60**, 566–593 (2018).
5. Gunasekar, G. H., Park, K., Jung, K. D. & Yoon, S. Recent developments in the catalytic hydrogenation of CO2 to formic acid/formate using heterogeneous catalysts. *Inorg. Chem. Front.* **3**, 882–895 (2016).
6. Preti, D., Resta, C., Squarcialupi, S. & Fachinetti, G. Carbon dioxide hydrogenation to formic acid by using a heterogeneous gold catalyst. *Angew. Chemie - Int. Ed.* **50**, 12551–12554 (2011).
7. Filonenko, G. A., Vrijburg, W. L., Hensen, E. J. M. & Pidko, E. A. On the activity of supported Au catalysts in the liquid phase hydrogenation of CO2 to formates. *J. Catal.* **343**, 97–105 (2016).
8. Schaub, T. & Paciello, R. A. A process for the synthesis of formic acid by CO2 hydrogenation: Thermodynamic aspects and the role of CO. *Angew. Chemie - Int. Ed.* **50**, 7278–7282 (2011).
9. V. R. Ferro et al. Integration of COSMO-based methodologies into commercial process simulators: Separation and purifcation of reuterin". In: AIChE Journal 58.11 (Nov. 2012), pp. 3404. doi: 10.1002/AIC.13746.
10. Jingli Han et al. \Parameterization of COSMO-RS model for ionic liquids". In: Green Energy and Environment 3.3 (2018), doi: 10.1016/j.gee.2018.01.001
11. Andreas Klamt, Frank Eckert, and Wolfgang Arlt. \COSMO-RS: An alternative to simulation for calculating thermodynamic properties of liquid mixtures". In: Annual Review of Chemical and Biomolecular Engineering 1 (2010), pp. 101, doi: 10.1146/annurev-chembioeng-073009-100903.
12. te Velde, G., Bickelhaupt, F. M., Baerends, E. J., Fonseca Guerra, C., van Gisbergen, S. J. A., Snijders, J. G., & Ziegler, T. (2001). Chemistry with ADF. *J. Comput. Chem.*, *22*(9), 931–967. doi:10.1002/jcc.1056
13. C.C. Pye and T. Ziegler, *An implementation of the conductor-like screening model of solvation within the Amsterdam density functional package*, Theoretical Chemistry Accounts 101, 396 (1999)
14. J.G. Boelhouwer. Nonsteady operation of trickle-bed reactors : hydrodynamics, mass and heat transfer". English. PhD thesis. Chemical Engineering and Chemistry, 2001. isbn: 90-386-2553-7. doi: 10.6100/IR549731.
15. Ahmet K. Avci 2.16 Catalysts". In: Comprehensive Energy Systems 2-5 (Jan.2018), pp. 475{ doi:10.1016/B978-0-12-809597-3.00235-2.
16. K.M.P. Eeten, van. Hydrodynamics of rotating multiphase flows". English. PhD thesis. Chemical Engineering and Chemistry, 2015. isbn: 978-90-386-3781-5.
17. M.M. de Beer. Hydrodynamics and heat transfer of single and multiphase flows in rotor-stator spinning disc reactors". English. Proefschrift. PhD thesis. Chemical Engineering and Chemistry, June 2016. isbn: 978-90-386-4075-4.
18. M. Meeuwse. Rotor-stator spinning disc reactor". English. PhD thesis. Chemical Engineering and Chemistry, 2011. isbn: 978-90-386-2450-1. doi: 10.6100/IR702643.
19. P. Granados Mendoza et al. Liquid{solid mass transfer to a rotating mesh electrode in a rotor-stator spinning disc configuration". In: International Journal of Heat and Mass Transfer 104 (Jan. 2017), pp. 650{657. issn: 0017-9310. doi: 10.1016/J.IJHEATMASSTRANSFER.2016.08.076.
20. Arnab Chaudhuri et al. Scale-Up of a Heterogeneous Photocatalytic Degradation Using a Photochemical Rotor Stator Spinning Disk Reactor". English. In: Organic Process Research & Development (Mar. 2022). issn: 1083-6160. doi: 10.1021/acs.oprd.2c00012.

7 Appendix Packed Bed Reactor

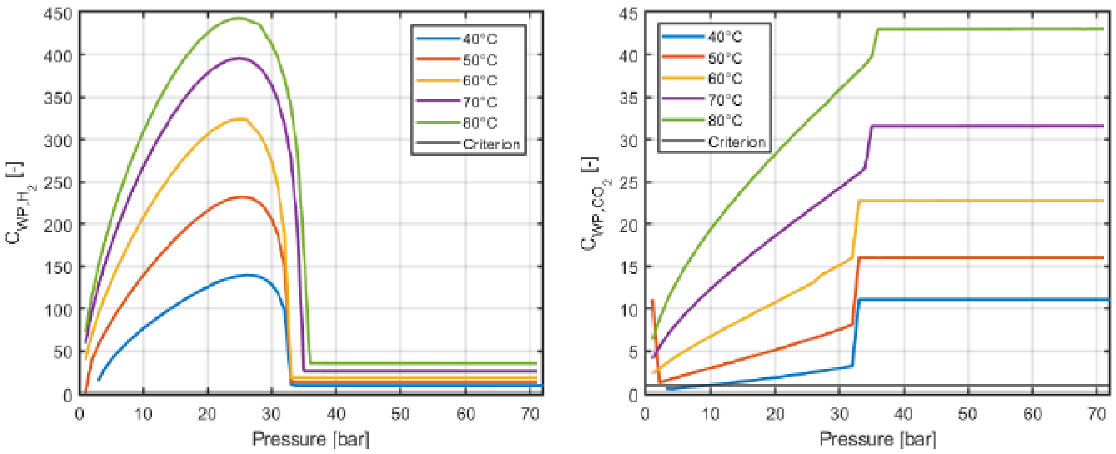

(a) H_2 (b) CO_2

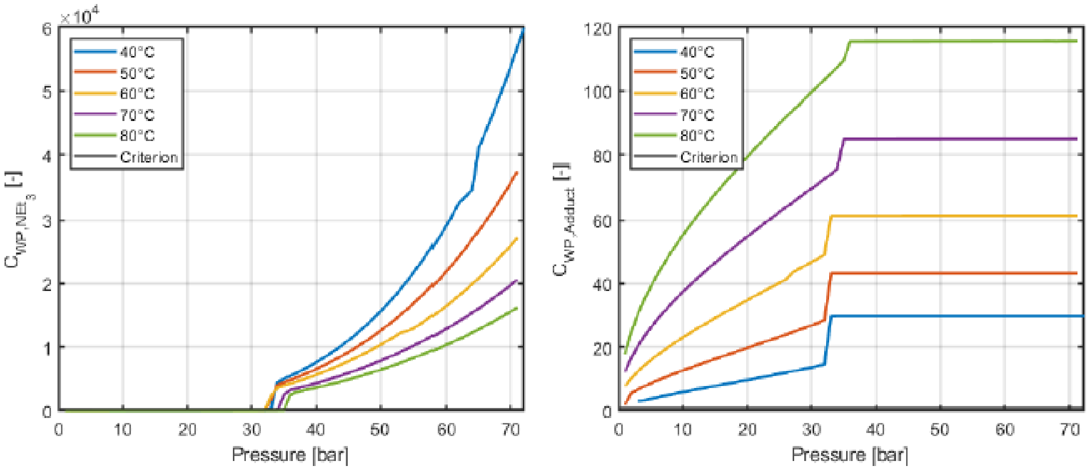

(c) NEt_3 (d) Adduct

Figure 22: Weisz-Prater for the reactants and product at different temperatures and pressures for the packed bed configuration.

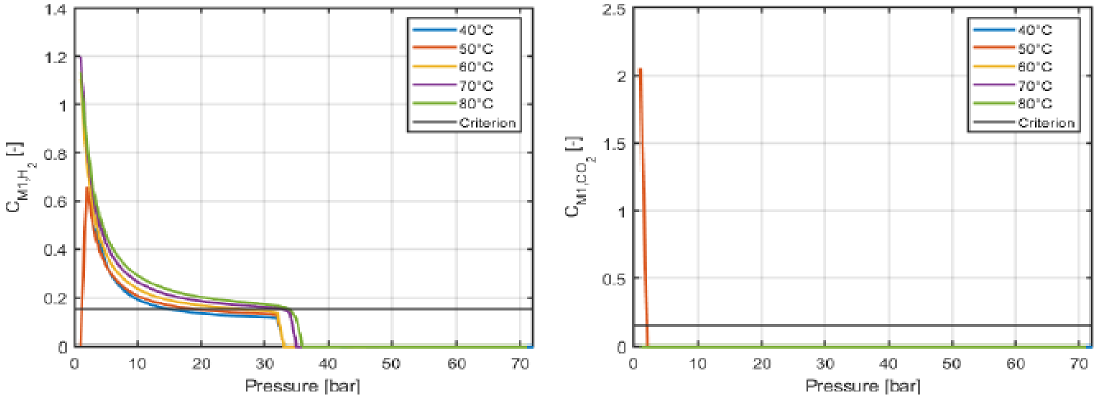

(a) H_2 (b) CO_2

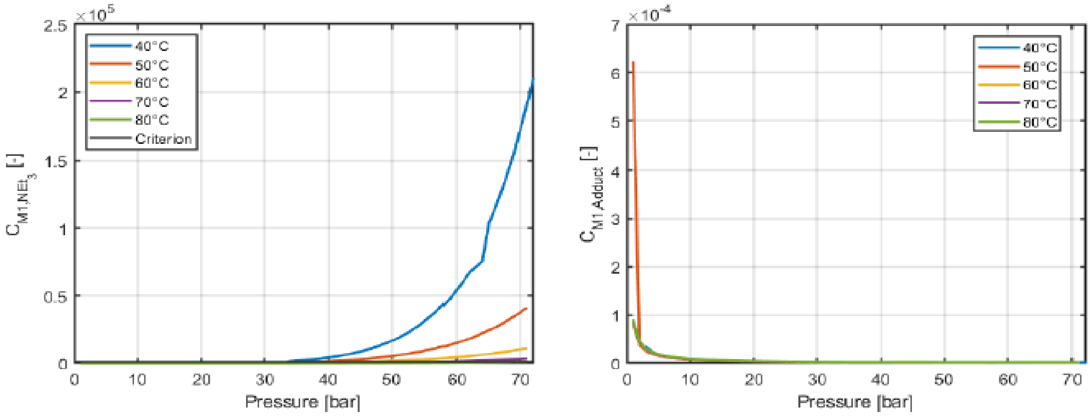

(c) NEt_3 (d) Adduct

Figure 23: First Mears criteria for the reactants and product at different temperatures and pressures for packed bed configuration.

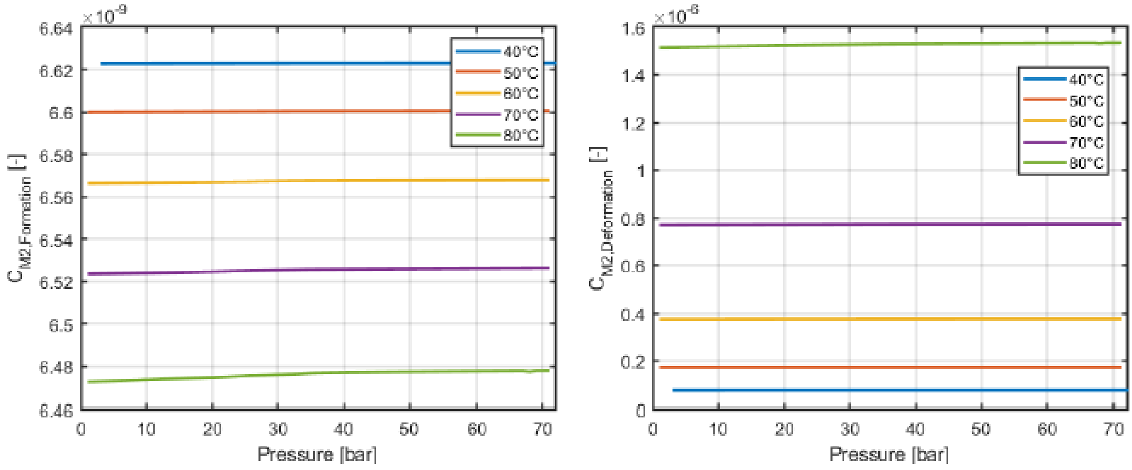

(a) Formation reaction (b) Decomposition reaction

Figure 24: Second Mears criterion for the packed bed reactor

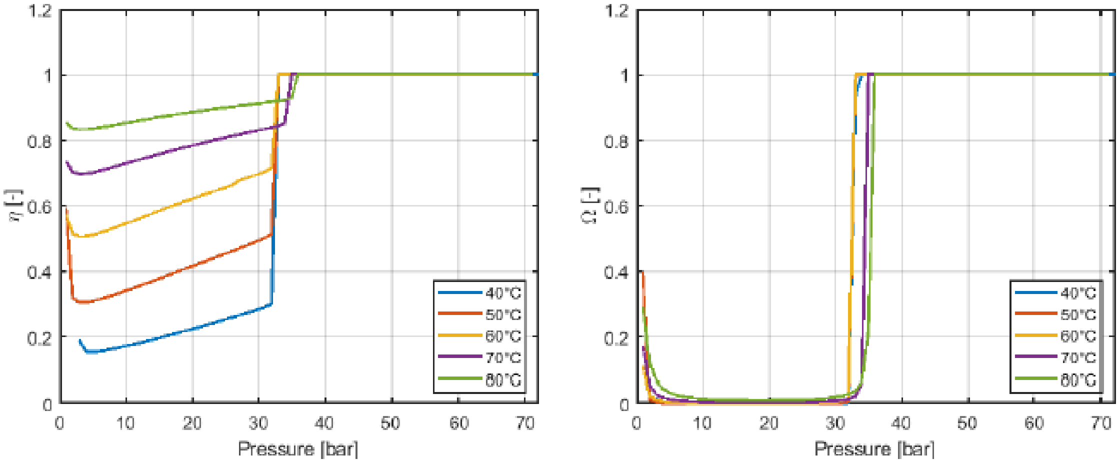

(a) Internal effectiveness factor (b) External effectiveness factor

Figure 25: Internal and external effectiveness factor for the packed bed reactor, figure based on the formation reaction

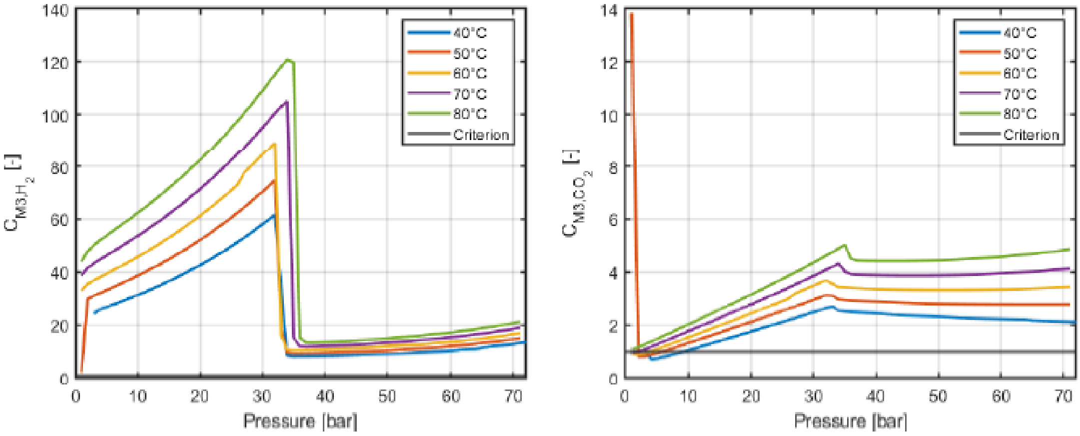

(a) H_2 (b) CO_2

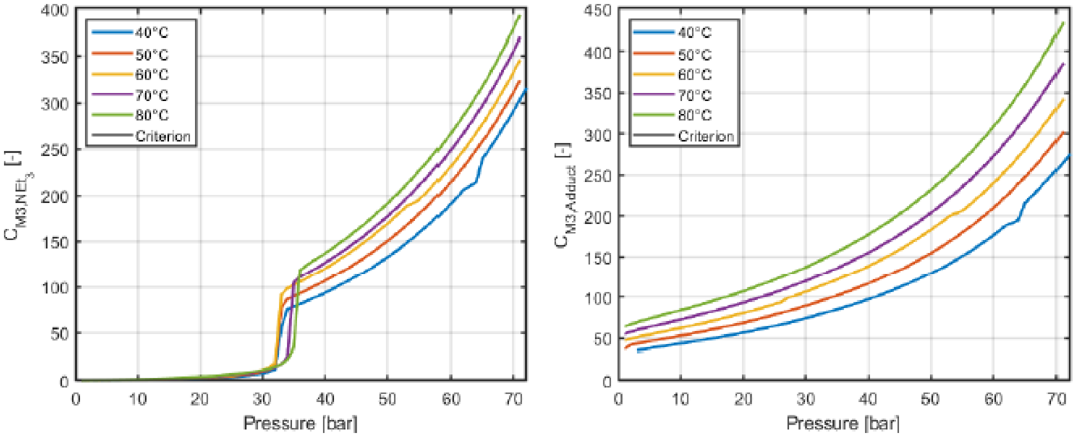

(c) NEt_3 (d) Adduct

Figure 26: Third Mears criteria for the reactants and product at different temperatures and pressures for the packed bed configuration.